

Instance-Aware Pseudo-Labeling and Class-Focused Contrastive Learning for Weakly Supervised Domain Adaptive Segmentation of Electron Microscopy

Shan Xiong, Jiabao Chen, Ye Wang, and Jialin Peng *Senior Member, IEEE*

Abstract—Annotation-efficient segmentation of the numerous mitochondria instances from various electron microscopy (EM) images is highly valuable for biological and neuroscience research. Although unsupervised domain adaptation (UDA) methods can help mitigate domain shifts and reduce the high costs of annotating each domain, they typically have relatively low performance in practical applications. Thus, we investigate weakly supervised domain adaptation (WDA) that utilizes additional sparse point labels on the target domain, which require minimal annotation effort and minimal expert knowledge. To take full use of the incomplete and imprecise point annotations, we introduce a multitask learning framework that jointly conducts segmentation and center detection with a novel cross-teaching mechanism and class-focused cross-domain contrastive learning. While leveraging unlabeled image regions is essential, we introduce segmentation self-training with a novel instance-aware pseudo-label (IPL) selection strategy. Unlike existing methods that typically rely on pixel-wise pseudo-label filtering, the IPL semantically selects reliable and diverse pseudo-labels with the help of the detection task. Comprehensive validations and comparisons on challenging datasets demonstrate that our method outperforms existing UDA and WDA methods, significantly narrowing the performance gap with the supervised upper bound. Furthermore, under the UDA setting, our method also achieves substantial improvements over other UDA techniques.

Index Terms—Domain adaptive segmentation, weak supervision, electron microscopy, mitochondria segmentation, pseudo-labeling

I. INTRODUCTION

This work was partly supported by the National Natural Science Foundation of China under Grant 12471498 and the Natural Science Foundation of Xiamen under Grant 3502Z202373042. (Corresponding author: Jialin Peng)

Shan Xiong is with the College of Computer Science and Technology, Huaqiao University, Xiamen 361021, China

Jiabao Chen is the College of Computer Science and Technology, Huaqiao University, Xiamen 361021, China.

Ye Wang is with Finance and Economics College, Jimei University, Xiamen, China.

Jialin Peng is with Fujian Key Lab of Big Data Intelligence and Security and the College of Computer Science and Technology, Huaqiao University, Xiamen 361021, China (e-mail: jialinpeng@hqu.edu.cn, 2004pjl@163.com).

Recent advancements in various 3D electron microscopy (EM) technologies, such as transmission electron microscopy (TEM), serial block face-scanning electron microscopy (SBF-SEM), and focused ion beam-scanning electron microscopy (FIB-SEM), enable researchers to obtain high-resolution information about intracellular structures. Consequently, there is a pressing need for automatic segmentation of subcellular organelles [1], *e.g.*, mitochondria [2], [3], from large-scale sequential cross-sectional EM images. Such segmentation can provide critical information for research in biological and neuroscience [3], [4]. For instance, upon reconstructing over 135,000 mitochondria, Liu *et al.* [5] found that fear conditioning not only increases the mitochondrial count but also leads to a reduction in their size. This highlights the necessity of precise instance-level segmentation of mitochondria for meaningful insights into cellular responses.

Despite the significant advancements in deep learning methods [6]–[11] for image segmentation, training supervised learning methods relies strongly on large-scale *domain-specific training data* with *high-quality fine-grained annotations*. However, collecting pixel-wise expert annotations for biomedical images [12], [13], especially for cellular EM images that often feature numerous small object instances, is prohibitively expensive. Furthermore, the performance of supervised models can significantly decline [14], [15] when there is a discrepancy between the distributions of the training and testing data. For EM image segmentation, EM images acquired from diverse tissues usually exhibit considerable style/acquisition variations, along with structural/biological variations, leading to significant domain shifts. Biological studies [4], [16] have demonstrated that the morphology of mitochondria can vary significantly across different cell types. The high cost of manual annotation and the domain shifts among different EM datasets present major challenges for fully supervised segmentation and for deploying well-trained segmentation models across varying domains.

To reduce annotation burden and reuse well-trained models, researchers have developed various domain-adaptation methods [17]–[22]. These methods aim to adapt a model that has been well-trained on a labeled source domain to a different target domain. Unsupervised Domain Adaptation (UDA) [17] is a widely considered setting that operates under the as-

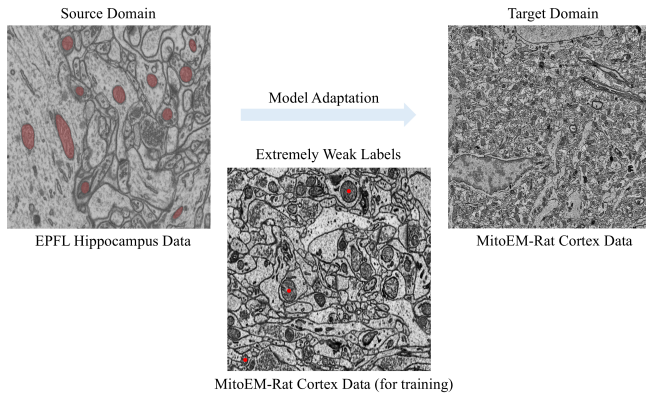


Fig. 1. Weakly-Supervised Domain Adaptation (WDA) for mitochondria segmentation in EM images. Sparse center points on a few object instances are utilized as the weak labels on target training data.

sumption that no labels are available in the target domain, thus eliminating the annotation burden on the target domain. However, despite significant research efforts, a substantial performance gap persists between the UDA and supervised methods for most tasks. This gap presents challenges when applying UDA in biomedical applications [12], [14], where segmentation performance is critically important. In practical applications, it is essential to find an effective balance between segmentation accuracy and annotation cost.

To address these relatively less-explored issues, we consider weakly supervised domain adaptation (WDA), which allows extremely weak labels on the target training data as illustrated in Fig. 1. A significant challenge associated with pixel-wise annotation of EM is that it requires extensive expert knowledge to *delineate the boundaries of mitochondria accurately* and to *annotate all instances of these organelles*. To minimize the burden of annotations required for segmenting numerous organelle instances, we consider sparse points—specifically, center points on a few object instances, as introduced in our previous study [23]—as weak labels. This form of weak annotation reduces over 95% of the time required for pixel-wise annotations and reduces 74% of the time required for full point annotations [12]. More importantly, only annotating partial center points demands significantly less expertise and knowledge, making it particularly beneficial for microscopy image annotation. It is worth noting that point annotation represents an extreme version of the commonly used scribble and bounding box annotations. However, it is significantly easier to annotate a large number of small object instances compared to using scribbles or bounding boxes. Additionally, annotating center points is a more straightforward process compared to placing effective scribbles or bounding boxes, which typically require more specialized domain knowledge and a deep understanding of the specific target object.

Given partial labels, self-training with pseudo-labels is typically used to leverage unlabeled data. While most existing methods concentrate on selecting confident pseudo-labels to minimize error accumulation, less attention has been given to the diversity of the pseudo-labels. This diversity, or the representativeness of pseudo-labels, is crucial for avoiding bias in pseudo-labels. The most common strategies for quantifying

the confidence of pseudo-label selection include pixel-wise thresholding based on the maximum softmax prediction scores of the model or assessing the entropy of softmax prediction scores across all classes. Typically, a high confidence threshold (e.g., 0.95) is needed to exclude more erroneous pseudo labels and reduce the negative impacts of error accumulation. However, a high threshold will result in the exclusion of correct pseudo-labels that have relatively lower confidence scores, ultimately diminishing the representativeness of the labeled regions and compromising the model’s ability to generalize. Besides the difficulty in setting thresholds, the pixel-wise pseudo-label selection for the segmentation task, which involves structural prediction, is another limitation.

This study presents a novel multitask learning-based WDA method that leverages *cross-task teaching*, innovative *semantic pseudo-labeling*, and *class-focused contrastive learning* to effectively address the challenges associated with employing the incomplete and imprecise point annotations. Since it is posited that partial point annotations provide more informative guidance for detection tasks than for segmentation tasks, we augment the segmentation task with an auxiliary center-point detection task and conduct cross-task teaching to enhance the accuracy of mitochondria instance localization and the selection of semantic pseudo-labels. In light of the inherent limitations associated with pixel-wise pseudo-label selection and the difficulties in establishing a reliable confidence threshold, this work introduces a simple yet effective semantic selection strategy termed *instance-aware pseudo-labels (IPL)*. This approach aims to preserve diversity among pseudo-labels while ensuring their reliability. It is based on the observation on the observation that the appearance of pixels within each mitochondria instance typically demonstrates a high degree of similarity, while the backgrounds present diverse appearances. Our instance-aware rectification allows pseudo-labeling pixels with relatively lower prediction scores as long as they belong to a pseudo-labeled mitochondria instance. To enhance feature-level domain alignment and improve the compactness of category feature representations, we introduce a contrastive learning with class-focused prototypes that are different from those in previous methods [24], [25]. We observed that the foreground class, specifically mitochondria in EM images, usually exhibits more similarity than the more complex background class. Concretely, we compute the foreground prototype as a mix of features from both the source domain and target domain, and a mix of features from the labeled sparse points and confident pseudo-labeled regions. Moreover, we further strengthen the detection training with supervision derived from the segmentation predictions. Different from other domain adaptation methods [12], [18], [26], our method circumvents the need for adversarial training, which is often challenging and prone to instability.

The main contribution of our study is as follows: 1)

- 1) This study develops an effective WDA method that significantly outperforms UDA methods and demonstrates comparable performance to supervised methods with minimal annotation efforts and knowledge.
- 2) Rather than using pixel-wise pseudo-label selection, this study proposes a simple yet effective instance-aware

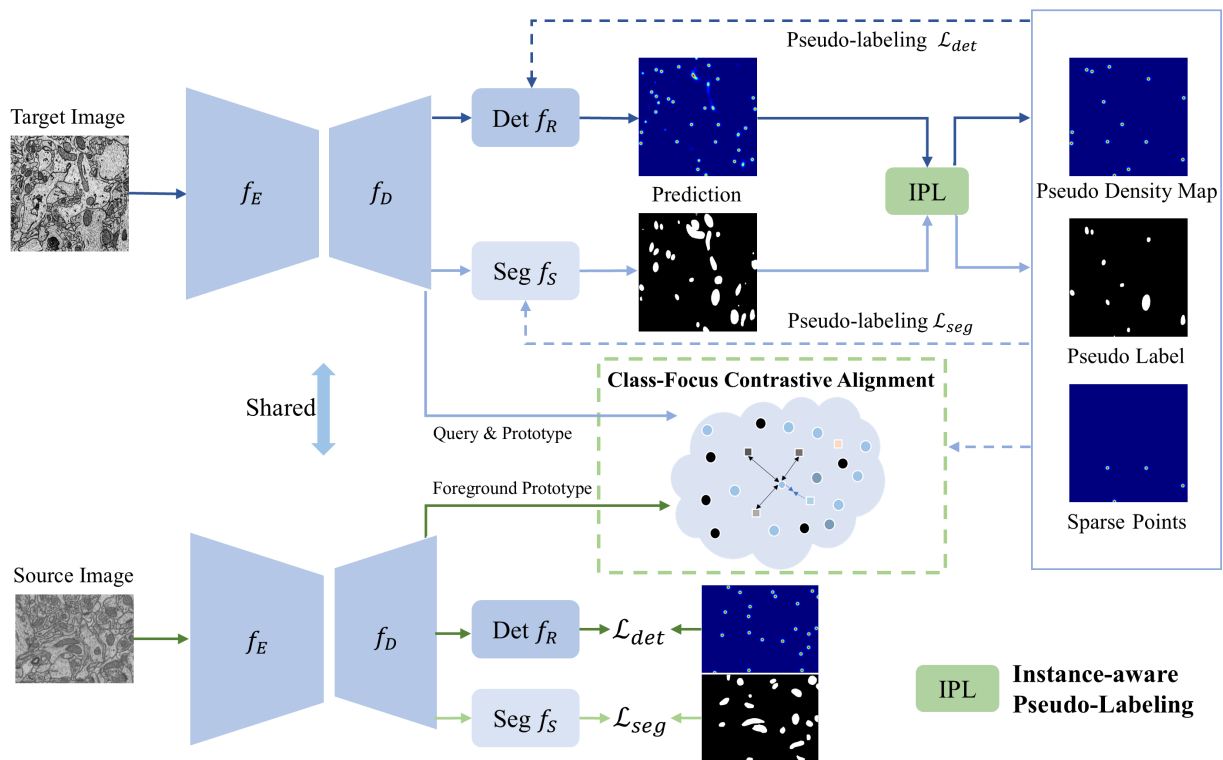


Fig. 2. Overview of the proposed method for weakly-supervised cross-domain adaptation. Under a multitask learning framework, an auxiliary center detection task is utilized to achieve instance-aware pseudo-label selection for the self-training on the segmentation head. class-focused conservative learning through pixel-to-prototype alignment is introduced to conduct feature-level domain alignment and improve the compactness of category feature representations.

pseudo-labeling strategy.

- 3) A class-focused contrastive learning approach has been introduced to effectively learn domain-invariant features.

II. RELATED WORK

A. Unsupervised Domain Adaptation

Deep learning models trained on a specific domain often suffer from significant performance degradation when tested on datasets with shifted distributions. Although foundation models like the Segment Anything Model (SAM) [27] and its medical variants, such as Med-SA [28], have shown strong zero-shot generalization capabilities with object-wise prompts, they still face considerable challenges in biomedical applications due to persistent performance degradation under a large domain gap and the reliance on object-wise prompts. Domain adaptation techniques aim to adapt a well-trained source model to perform well on a related but different target domain, often with limited or no labeled data. Typical approaches seek to learn a proper feature space [14] and align the (marginal) distributions of latent representations from source and target domains by minimizing distribution discrepancy loss (e.g., maximum mean discrepancy [29]), conducting adversarial alignment [18], [26], [30] and contrastive alignment [25], [31], or performing style transfer in the image space [31], [32]. For example, the AdaptSegNet in [26] aligns domains by conducting adversarial learning in the output space. For EM segmentation, the DAMT-Net [18] conducts domain alignment in label space, feature space, and image space. Recently,

self-training or pseudo-labeling—techniques commonly used in semi-supervised learning—have also been introduced to boost the domain adaptation [19], [33]. In this process, self-training directly estimates pseudo-labels on target domains and iteratively trains the segmentation model with both ground truth source labels and target pseudo-labels. An example of approaches in this class is the SAC [19], which utilizes pixelwise pseudo-labeling within a mean teacher framework. For sequential EM image segmentation, DA-ISC [22] takes advantage of intersection consistency to generate pseudo labels for adjacent sections. A closely-related method to ours is the CAFA [21] method, which combines pixelwise pseudo-labeling with contrastive alignment, using source domain prototypes of all categories to guide feature alignment. However, due to the domain gap, especially the significant distribution shift in background class, using the source prototype of all class tend to produce suboptimal results.

B. Weakly Supervised Domain Adaptation

Recently, various weak labels, such as image-level labels [24], [34], scribbles/coarse labels [24], points [24], [35], and bounding-boxes [36], have been explored for cross-domain segmentation/detection. While image-level labels only provide categorical information, scribbles, bounding boxes, and points also offer information about the location and appearance of objects. Consequently, image-level labels are typically used in multi-class semantic segmentation [24], [34]. However, our focus is on mitochondria segmentation, where categorical

information does not significantly enhance the identification of the mitochondria instances. Das *et al.* [24] considered using a single point for each semantic class in multi-class semantic segmentation, whereas we consider using sparse points on a few instances to facilitate the segmentation of numerous organelle instances. They also used the features derived from weak labels as anchors/prototypes to guide contrastive feature learning. However, with point annotations, the annotated areas are quite limited, and the weak-label-based anchor may be misleading, especially in complex biomedical image segmentation tasks. A closely-related work is the WDA-Net *et al.* [12], which introduces sparse points as weak labels and employs an adversarial domain alignment. They also use self-training, but with a pixel-wise entropy-based pseudo-label estimation strategy.

III. METHODOLOGY

A. Overview

Problem setting. In the WDA setup, we are given the densely labeled source data $\mathcal{D}^s = \{(x^s, y^s)\}$, where $x^s \in \mathbb{R}^{H \times W}$ is a source image and $y^s \in \mathbb{R}^{H \times W}$ is its corresponding label image, and a weakly-labeled target dataset $\mathcal{D}^t = \{(x^t, \tilde{c}^t)\}$, where $\tilde{c}^t \in \{0, 1\}^{H \times W}$ is the dot label only taking 1 on the sparsely annotated points. Additionally, we denote the dot label of y^s as $c^s \in \{0, 1\}^{H \times W}$, which only takes 1 on the center point of each object instance in y^s , and we further denote the corresponding density map of c^s as d^s that can be obtained through the convolution of a Gaussian kernel k_σ with the dot label $d^s = k_\sigma * c^s$, in which σ (e.g., 11) is the kernel bandwidth. The goal of the WDA is to learn a segmentation model that adapts well to the target domain.

Model overview. An overview of our model is demonstrated in Fig. 2, in which we conduct multitask learning with a cross-task teaching mechanism. Our model takes an encoder-decoder architecture $f_D \circ f_E$ with a segmentation head f_S and a regression-based detection head f_R , where f_E is the shared feature encoder and f_D is the shared base decoder. The segmentation sub-network $F_S = f_S \circ f_D \circ f_E$ predicts the probabilistic segmentation map, and the detection sub-network $F_D = f_R \circ f_D \circ f_E$ predicts the density map of the center points of target object instances. F_S and F_D are jointly pre-trained on the labeled source domain. At the model adapting stage, the training of both F_S and F_D is supervised with source labels, target sparse point labels, and target pseudo labels. During the training process, the output of the detection sub-network F_D is used to guide the selection of reliable and diverse pseudo-labels for the segmentation. Additionally, the segmentation sub-network F_S is also guided by a contrastive alignment loss, which significantly helps domain-invariant feature learning.

B. Auxiliary detection task

Compared to the complicated dense segmentation task, detecting instance centers is much easier, particularly with sparse point annotations. Moreover, the outputs from the detection can be effectively utilized to substantially enhance the segmentation of mitochondrial instances. This insight leads

us to investigate a unified learning framework that encompasses both segmentation and detection tasks. For center-point detection, we adopt the density map regression strategy [37]. Notably, although the annotated sparse points provide minimal additional information to the dense segmentation task, they provide much richer information to the center-point detection task.

Detection pseudo-label learning. To improve the source detection model with partial point annotations on the target domain, we follow the self-training strategy [38] and iteratively train our detection model using a combination of ground-truth sparse point labels and progressively refined pseudo-labels. The cornerstone of this self-training process lies in the effective selection of pseudo-labels, which is critical for improving model performance.

$$\mathcal{L}_{det} = \frac{1}{|\mathcal{D}^s|} \sum_{x^s} L_2(F_D(x^s), d^s) + \frac{1}{|\mathcal{D}^t|} \sum_{x^t} L_2(F_D(x^t), \hat{d}^t) \quad (1)$$

where L_2 is the standard least square loss, \hat{d}^t is the density map of the union set of ground-truth sparse points and the estimated pseudo-label points. More specifically, in each self-training iteration, we first estimate the total number of mitochondria instances by summation of the predicted density map. Then, we select a proportion of $\beta\%$ (e.g., 20%) more points that have the highest responses in the predicted density map as the additional pseudo-label points. Given a density map, candidate points with the highest responses are local maxima points and can be obtained with standard Non-Maxima Suppression (NMS) [37]. To suppress noises in the predicted density map, we ensemble the predictions of 5 differently augmented versions (e.g., flip, rotate, etc.) of the input. Ground-truth sparse points are always used as the supervision.

Thus, in each self-training iteration, we integrate the newly selected points with previously selected points as updated pseudo-labels and then construct new density maps to supervise the model training. For the target data, the L_2 loss \mathcal{L}_{det} is calculated exclusively on positive regions of \hat{d}^t and confident background regions inferred from the density map in the preceding self-training iteration. Our experimental setup involves training the detection model over four iterations, utilizing up to 80% of the center points. Additionally, by maintaining a shared architecture across most layers, the detection network F_D implicitly enhances the segmentation network F_S , enabling more accurate instance recognition.

C. Segmentation via instance-aware pseudo-labeling

Since we only have extremely limited point labels on the target training data, as demonstrated in Fig. 1, we train the segmentation sub-network F_S under the framework of self-training, which is guided by the detection prediction. A combination of the source dense labels, target point labels, and generated target pseudo-labels is utilized to supervise the model training.

$$\mathcal{L}_{seg} = \frac{1}{|\mathcal{D}^s|} \sum_{x^s} L_{CE}(p(x^s), y^s) + \frac{1}{|\mathcal{D}^t|} \sum_{x^t} L_{CE}(p(x^t), \hat{y}^t) \quad (2)$$

where L_{CE} is the standard cross-entropy loss, $p(x) = F_S(x)$ is the predicted segmentation, \hat{y}^t is a fusion of the estimated pseudo-labels and ground truth point annotations.

Instance-aware pseudo-label selection. Rather than relying on a high threshold for pixel-wise pseudo-label filtering, we select confident pseudo-labels on an instance-wise basis to preserve the diversity of pseudo-labels. Specifically, we propose to leverage the output of the detection head F_D to guide the pseudo-label selection in the segmentation process. During each self-training iteration, we first estimate the total number of mitochondria instances by summation of the predicted density map. Next, we extract a specified proportion (e.g., 50%) of the most confident local maxima based intensity values from the density map, denoting this set of selected points as Ω . The ground-truth sparse points are incorporated as confident points as well. Subsequently, we identify the connected regions associated with these confident points in the current binary segmentation output to serve as our pseudo labels for mitochondria instances.

$$\hat{y}^t = \text{IPL}(\Omega, \text{TH}(p(x^t))) \quad (3)$$

where Ω is the selected confident centers, $\text{TH}(p(x^t))$ denotes the binarization of the probabilistic segmentation prediction of x^t at a predefined threshold (for instance, 0.7 in our experiments), $\text{IPL}(\cdot, \cdot)$ signifies the instance-aware pseudo-label selection that is achieved through selecting the connected regions associated with Ω from $\text{TH}(p(x^t))$. Here, we refer to these selected connected regions as *pseudo-label instances*. In our experiment setup, we conduct three iterative rounds of self-training. During the first iteration, we restrict ourselves to using only the ground-truth sparse points as the confident points. In the subsequent second and third rounds, we expand our selection to 50% and 95% of the most confident points, respectively, to select pseudo-label instances. To further enhance the accuracy of segmentation, we also incorporate a filtering process to eliminate false positives, relying on the predictions made by the detection head.

D. Class-focused contrastive alignment

Contrastive feature alignment. To enhance feature-level domain alignment and improve the compactness of category feature representations, we augment our WDA with class-focused pixel-to-prototype contrastive learning. Unlike pixel-to-pixel contrast, pixel-to-prototype contrast with well-defined prototypes usually yields greater robustness and computational efficiency. In this study, we exploit multiple prototypes for each class. Let $z^t = f_D \circ f_E(x^t)$ denote the feature maps derived from the target domain input x^t . For each class c , we extract a set of pixel-wise queries $\mathbb{Q}^c = \{z_{ic}^t\}_{i=1}^N$ solely from the target domain, and a set of class prototypes $\mathbb{P}^c = \{\mu_k^c\}_{k=1}^{K_c}$ from the source and target domains as well as their (weighted) mean prototype $\bar{\mu}^c$. Notably, we have observed that the foreground class in different EM images generally exhibits higher intra-class similarity than the more complex and variable background class. Therefore, we utilize foreground prototypes estimated from features from both the

source and target domains, while the background prototypes are derived solely from target domain features.

To achieve inter- and intra- domain alignment, we utilize a contrastive loss designed to align the class-specific queries with the class mean prototype while ensuring that they are dissimilar. This strategy not only facilitates feature discrimination but also fosters effective domain adaptation across different categories with our class-focused contrastive alignment.

$$\mathcal{L}_{contra} = -\frac{1}{NC} \sum_{c=0}^{C-1} \sum_{i=1}^N \log \frac{\exp(z_{ic}^t \cdot \bar{\mu}^c / \tau)}{\exp(z_{ic}^t \cdot \bar{\mu}^c / \tau) + \sum_{l \neq c} \sum_{k=1}^{K_l} \exp(z_{ic}^t \cdot \mu_k^l / \tau)} \quad (4)$$

where the temperature τ is to control the softness of the softmax function, and C is the category number. For binary segmentation, $C=2$.

Query samples from target domain. In this study, we focus solely on sampling queries from the target domain. For each class, our query set is composed of both hard samples and easy samples, represented as $\mathbb{Q}^c = \mathbb{Q}_{hard}^c \cup \mathbb{Q}_{easy}^c$.

Easy queries are features of the pixels that not only have the label or pseudo-label c , but also demonstrate a sufficiently high level of confidence.

$$\mathbb{Q}_{easy}^c = \{z_i^t | \hat{y}_i^t = c, p_i^t > \delta_e\} \quad (5)$$

where p_i^t refers to $p(x^t)$ at pixel i .

Hard queries are features of the pixels whose labels/pseudo-labels are c but show low confidence.

$$\mathbb{Q}_{hard}^c = \{z_i^t | \hat{y}_i^t = c, p_i^t < \delta_h\} \quad (6)$$

In our experiments, we set $\delta_e = 0.95$ and $\delta_h = 0.80$. For each class, to reduce computation complexity, we only sample $N=1024$ queries, which contain 512 hard samples and 512 easy samples, in each batch.

Class-focused prototypes. Since the foreground class, specifically mitochondria in EM images, usually exhibits higher similarity over different domains than the complicated background class, we introduce significantly different prototypes from that in previous methods and focus on the inter-domain alignment of the foreground class.

For the foreground class ($c=1$), the set of foreground prototypes \mathbb{P}^1 contains three types of prototypes: 1) the source prototype μ_s^1 derived from the features of foreground class pixels in the source images, 2) the target label prototype μ_t^1 estimated using the ground-truth point labels of target images, 3) the target pseudo-label prototype μ_{pl}^1 estimated using pseudo-labels assigned to the target images. More specifically, both the source prototypes μ_s^1 and the target label prototype μ_t^1 are calculated by averaging the features of the correctly labeled pixels.

$$\mu_k^1 = \frac{\sum_i z_i^k \mathbb{1}[y_i^k = 1] \mathbb{1}[\hat{p}_i^k > \delta_e]}{\sum_i \mathbb{1}[y_i^k = 1] \mathbb{1}[\hat{p}_i^k > \delta_e]}, \mu_{pl}^1 = \frac{\sum_i z_i^t \mathbb{1}[\hat{y}_i^t = 1]}{\sum_i \mathbb{1}[\hat{y}_i^t = 1]} \quad (7)$$

where $k \in \{s, t\}$, and $\mathbb{1}[\cdot]$ is the indicator function. While the source foreground prototype μ_s^1 and μ_t^1 guide cross-domain feature alignment, μ_t^1 and μ_{pl}^1 guide compact feature learning,

which is also crucial for improving performance in the target domain.

For the background class ($c=0$), we have two types of prototypes: 1) target pseudo-label prototype μ_{pl}^0 estimated using pseudo-labels of the target images, 2) 2 clusters of features at pseudo-labeled regions of target images, which are computed used k-means and updated every 1000 iterations in the experiments. Note that prototypes of background features of the source domain are not considered in our method due to the large distribution shift for the background class.

E. Training objectives

An illustration of our whole model is in Fig. 2. The overall loss for model training is given as,

$$\mathcal{L}_{obj} = \mathcal{L}_{seg} + \lambda_1 \mathcal{L}_{det} + \lambda_2 \mathcal{L}_{contra} \quad (8)$$

in which λ_1 and λ_2 are non-negative trade-off parameters. At the testing stage, no user annotation is needed.

IV. EXPERIMENTS

A. Datasets and metrics

EPFL Hippocampus Data. This dataset was scanned with a focused ion beam scanning electron microscope (FIB-SEM) [2] in a resolution of $5 \times 5 \times 5 \text{ nm}^3$, representing tissues from the mouse CA1 hippocampus region. This dataset was split into two subsets, each of which contains 165 image slices of size $768 \times 1,024$, for training and testing, respectively.

MitoEM-R Cortex Data. The MitoEM Dataset [13] constrains two subsets. The MitoEM-R subset was scanned using a multi-beam scanning electron microscope (SEM) at a resolution of $8 \times 8 \times 30 \text{ nm}^3$, representing Layer II/III in the primary visual cortex of an adult rat. This dataset was split into a subset of size $400 \times 4096 \times 4096$ and a subset of size $100 \times 4096 \times 4096$ for training and testing, respectively. To train our model, we just randomly selected 40 slices from the training set as actual training data.

MitoEM-H Temporal Lobe Data. MitoEM-H is a subset of the MitoEM Dataset [13]. This dataset was taken from Layer II in the human temporal lobe at a resolution of $8 \times 8 \times 30 \text{ nm}^3$. This dataset was also split into a subset of size $400 \times 4096 \times 4096$ and a subset of size $100 \times 4096 \times 4096$ for training and testing, respectively. To train our model, we just randomly selected 40 slices from the training set as actual training data.

Metrics. To evaluate the segmentation performance, we use both Dice similarity coefficient (Dice), Aggregated Jaccard-index (AJI) [39], and Panoptic Quality (PQ) [40] as the measures. Notably, AJI and PQ are instance-level measures.

Let P and G represent the predicted segmentation and the ground truth segmentation, respectively. The Dice coefficient can be mathematically defined as follows,

$$\text{Dice}(P, G) = \frac{2|P \cap G|}{|P| + |G|}. \quad (9)$$

Let G^j represent the j th instance (i.e., mitochondrion) in the set G , with a total of M instances. Similarly, P^j

denotes the j th instance in the set P . The measure AJI is mathematically defined as follows,

$$\text{AJI}(P, G) = \frac{\sum_{j=1}^M |P^j \cap G^{j^*}|}{\sum_{j=1}^M |P^j \cup G^{j^*}| + \sum_{i \in \text{FP}} |P^i|}, \quad (10)$$

where j^* refers to the index of the matched instance in P with maximal overlapping with G^j ; false positive (FP) refers to the set of instances in P that lack corresponding ground truth mitochondria in G .

The PQ is essentially a composite measure that evaluates detection accuracy and segmentation quality based on true positives (TP) [40]. Let FN represent the set of false negatives. The PQ is mathematically defined as follows,

$$\text{PQ}(P, G) = \frac{\sum_{j \in \text{TP}} \text{IOU}(P^j, G^{j^*})}{2|\text{TP}| + |\text{FP}| + |\text{FN}|}, \quad (11)$$

where $\text{IOU}(P^j, G^{j^*}) = |P^j \cap G^{j^*}| / |P^j \cup G^{j^*}|$.

B. Implementation details

For fair comparison with existing methods, we use the same network architecture as the WDA-Net in [12]. We implemented models with Pytorch and trained models with one GTX 3060 GPU of 12 GB memory. The widely-used SGD optimizer was used for model training with an initial learning rate of 5×10^{-5} and a batch size of 1. The training run for a maximum of 100,000 iterations, using randomly cropped patches of size 512×512 as input. We used polynomial decay of power 0.9 to control the learning rate decay. The same data augmentations as the WDA-Net were used. We set $\lambda_1=1 \times 10^{-2}$ and $\lambda_2=5 \times 10^{-3}$.

C. Comparison with the State-of-the-Art methods

We compare our method, including its UDA version, with the State-of-the-Art (SOTA) UDA methods (AdaptSegNet [26], DAMT-Net [18], SAC [19], UALR [20], DA-ISC [22], CAFA [21], WDA-Net (UDA) [12]), SOTA WDA method (WDA-Net (15%) [12]), and the Oracle model trained with full supervision. Among the UDA methods, DA-ISC [22], CAFA [21] are 2.5D methods that take multiple slices as input, while others, including our model, simply conduct 2D segmentation. We also compare our method with typical foundation models, including SAM [27], Med-SA [28], and their interactive versions, i.e., SAM (Interact), and Med-SA (Interact), which take center-points of all mitochondria instances as user prompts. Note that SAM was trained on billion-scale datasets and the Med-SA is an adapted version of SAM using medical datasets.

Table I presents the comparison results across three domain adaptation scenarios: EPFL Hippocampus \rightarrow MitoEM-R, MitoEM-R \rightarrow MitoEM-H, and MitoEM-H \rightarrow MitoEM-R. Notably, our approach, leveraging only 15% center point annotations, achieves a very small performance gap of 1% in Dice for the EPFL Hippocampus \rightarrow MitoEM-R task, 3.3% for MitoEM-R \rightarrow MitoEM-H, and 0.4% for MitoEM-H \rightarrow MitoEM-R when contrasted with the fully supervised upper-bound. These results indicate that utilizing sparse point weak labels, requiring minimal annotation effort, can effectively narrow

TABLE I

COMPARISON RESULTS ON EPFL HIPPOCAMPUS→MITOEM-R, MITOEM-R→MITOEM-H, AND MITOEM-H→MITOEM-R. IN DEFAULT, WE USE 15% OF CENTER POINTS AS THE WEAK ANNOTATION. FOR MITOEM, WE USE ONLY 1/10 OF MITOEM TRAINING SET FOR MODEL TRAINING.

Type	Methods	EPFL → R			R → H			H → R		
		Dice	AJI	PQ	Dice	AJI	PQ	Dice	AJI	PQ
NoAdapt	Source model	67.0	46.0	30.5	73.8	57.1	43.0	81.5	65.2	58.0
	SAM [27]	32.0	14.3	30.0	20.8	11.4	18.7	32.0	14.3	30.0
	SAM (Interact)	40.6	1.2	26.2	40.3	4.6	26.6	40.6	1.2	26.2
	Med-SA [28]	75.5	56.6	27.5	72.4	55.0	33.4	75.5	56.6	27.5
	Med-SA(Interact)	86.2	70.2	59.9	83.8	68.1	59.0	86.2	70.2	59.9
UDA	AdaptSegNet [26]	77.1	59.2	50.1	84.7	71.2	58.1	86.5	72.8	61.6
	DAMT-Net [18]	83.4	67.9	60.2	85.4	72.3	63.7	88.7	76.3	61.8
	SAC [19]	84.4	70.0	55.4	77.9	60.7	37.6	83.1	67.4	40.3
	UALR [20]	76.9	59.7	33.1	83.8	69.7	60.0	86.3	71.6	53.7
	DA-ISC [22](2.5D)	78.5	61.5	51.8	85.6	72.7	63.8	88.6	75.7	65.8
	CAFA [21](2.5D)	-	-	-	86.6	-	-	89.2	-	-
	WDA-Net(0%) [12]	86.1	71.5	61.2	85.5	72.3	60.6	88.2	74.5	59.0
	Ours(0%)	90.2	77.0	72.0	87.0	75.1	65.8	92.1	81.6	74.7
	WDA-Net(15%)	90.1	77.5	73.1	88.7	77.6	67.8	91.7	80.7	74.0
Ours(15%)	92.6	81.7	75.6	89.2	78.3	70.2	93.2	83.6	75.9	
Oracle	Supervised model	93.6	83.8	77.1	92.5	84.1	73.3	93.6	83.8	77.1

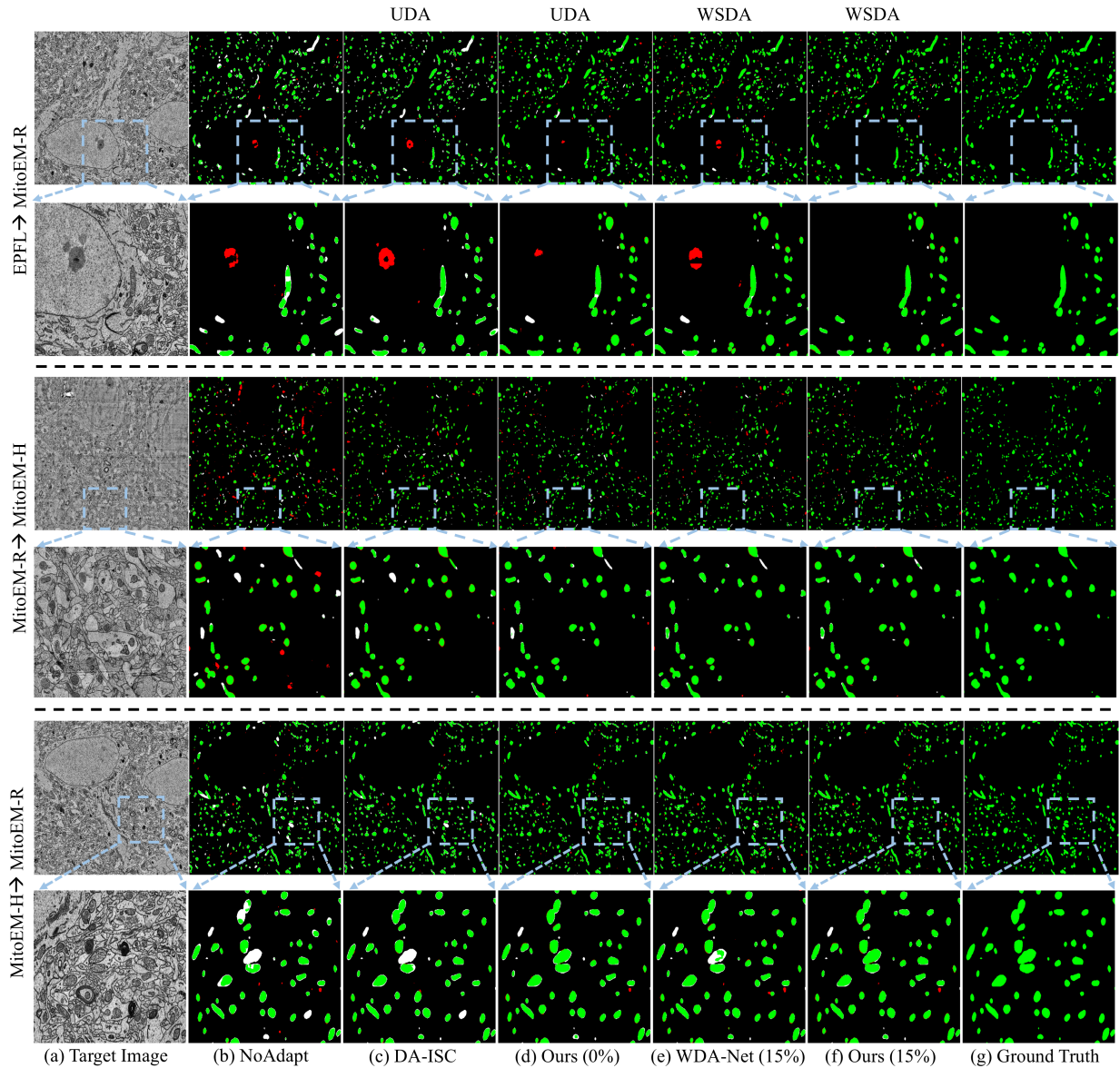


Fig. 3. Qualitative comparison results. Green: true positives; Red: false positives; White: false negatives.

TABLE II
ABLATION STUDY OF OUR MODEL (15%) ON EPFL HIPPOCAMPUS→MITOEM-R.

Setting	Detection Pseudo-Labeling	Segmentation Pseudo-Labeling	Class-focused Contrastive Learning	Dice (%)
I		✓ [†]		84.2
II	✓			88.8
III	✓	✓*		91.1
Full	✓	✓*	✓	92.6

[†] Threshold-based Pseudo-Labeling

* Instance-aware Pseudo-Labeling

the performance gap between supervised methods and domain adaptation methods. Additionally, our method significantly surpasses the current SOTA UDA methods. In particular, our model shows substantially enhanced performance over UDA methods when evaluated using instance-level metrics such as AJI and PQ. The UDA version of our approach also achieves the highest performance among the UDA methods, even demonstrating results that are competitive with WDA-Net (15%).

Moreover, with the same set of 15% center point annotations, our model consistently outperforms the WDA-Net (15%) across all metrics in all three tasks. Our model also outperforms its UDA version by 2.4% in Dice for EPFL Hippocampus→MitoEM-R, 2.2% for MitoEM-R→MitoEM-H, and 1.1% for MitoEM-H→MitoEM-R. A more detailed comparison of our method with WDA-Net under varying amounts of point annotations is shown in Table V and in the following section.

Besides, our model significantly outperforms the SAM model and its interactive version, which uses additional point prompts during the testing stage. Note that the low performance of SAM indicates the large domain gap between the EM data and its training data. Although Med-SA, the adapted version of SAM using medical data, shows improved performance, its performance still significantly lower than ours. Even with all center-points, Med-SA (Interact) still shows much lower performance than our method.

Visual comparison. Figure 3 visually compares our method with WDA-Net (15%), the UDA version of our method, and DA-ISC on all three tasks. As illustrated in Fig. 3, our method shows significantly reduced false positives (shown in Red) and false negatives (shown in White). As shown in the first row of the figures, our method demonstrates a stronger ability to successfully segment large mitochondria of irregular shapes.

D. Model analysis

Ablation study of key components. In this section, we first validate the effectiveness of our three key components: 1) auxiliary detection with pseudo-labeling, 2) instance-aware pseudo-labeling for segmentation, 3) class-focused contrastive learning. By comparing our full model with Model III in Table II, we have noticed a performance drop of 1.5% in the Dice coefficient when class-focused contrastive learning was removed. By further removing instance-aware pseudo-labeling, Model II resulted in a significant performance drop of 2.3% in Dice, while only using Pseudo-Labeling-based segmentation

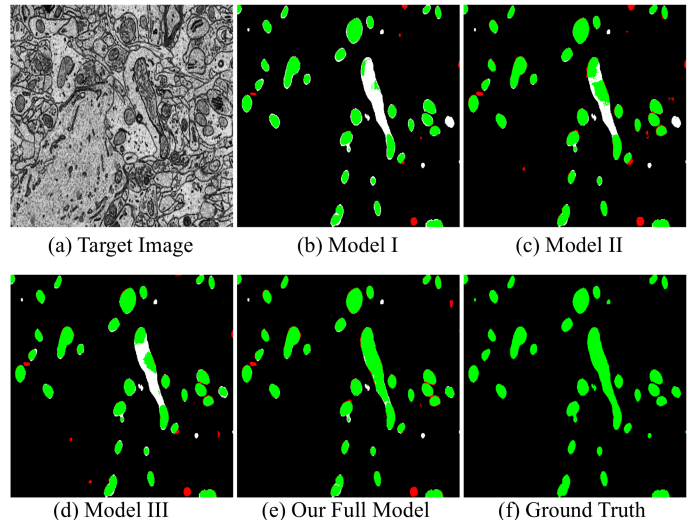


Fig. 4. Visual comparison of the ablated versions of our proposed approach.

TABLE III
PERFORMANCE COMPARISON USING DIFFERENT PSEUDO-LABEL SELECTION STRATEGIES FOR THE SEGMENTATION ON EPFL HIPPOCAMPUS→MITOEM-R.

Pseudo-Labeling for Segmentation	Dice (%)	PQ (%)
Threshold-based strategy	91.5	73.5
Entropy-based strategy [12]	91.6	73.6
Instance-aware based strategy (Ours)	92.6	75.6

further led to a significant performance drop of 3.8% in Dice. Our model achieves the best performance when all three components are integrated, demonstrating the effectiveness of our proposed approach. Figure 4 visually compares our model with its ablated versions, further indicating the effectiveness of the proposed components in our model.

Comparison of pseudo-labeling strategies. Table III presents a comparison of the proposed instance-aware pseudo-labeling with the widely used threshold-based method, which selects confident pseudo-labels based on predetermined thresholds, and the entropy-based strategy outlined in [12]. Our instance-aware strategy demonstrates superior performance, improving 1.0% in Dice and 2.0% in PQ over the entropy-based strategy. Additionally, it shows a gain of 1.1% in Dice and 2.1% in PQ when compared to the threshold-based method. All pseudo-labeling strategies were evaluated under the same settings to ensure a fair comparison.

Analysis of the class-focused contrastive alignment. In

TABLE IV

INFLUENCE OF DIFFERENT TYPES OF CONTRASTIVE ALIGNMENT. THE SEGMENTATION RESULTS OF THE MODEL WITH 15% SPARSE POINTS FOR EPFL HIPPOCAMPUS→MITOEM-R ARE REPORTED. WHILE SOURCE & TARGET REFERS TO CONDUCTING INTRA-DOMAIN CONTRASTIVE ALIGNMENT ON BOTH DOMAINS, SOURCE + TARGET REFERS TO CONDUCTING BOTH INTRA-DOMAIN ALIGNMENT ON THE TARGET DOMAIN AND INTER-DOMAIN ALIGNMENT ACROSS DOMAINS.

Contrast. Alignment	Setting	class-focus	Dice (%)
No Contrast	-	-	91.1
Intra-domain	Source only	-	91.4
	Target only	-	91.6
	Source & Target	-	91.9
Inter- & Intra- domain	Source + Target [†]	Background	91.9
	Source + Target [†]	Foreground	92.6

[†] Utilizing only target queries.

TABLE V

PERFORMANCE COMPARISON ON EPFL HIPPOCAMPUS→MITOEM-R WITH DIFFERENT AMOUNTS OF TARGET ANNOTATIONS, MEASURED IN DICE (%) PERFORMANCE.

Method	0%	5%	15%	50%	100%	Oracle
WDA-Net [12]	86.1	88.8	90.1	91.4	92.0	93.6
Ours	90.2	91.8	92.6	92.7	93.4	93.6

our model, we not only construct intra-domain contrastive learning on the target domain but also employ inter-domain contrastive alignment with a focus on the foreground class in a single contrastive loss. More specifically, the foreground prototype $\bar{\mu}^1$ fuses both source and target prototypes. Table IV compares our approach to five alternative settings: 1) no contrastive learning; 2) only intra-domain contrastive learning on the source domain; 3) only intra-domain contrastive learning on the target domain; 4) intra-domain contrastive learning on both the source and target domains with two separate losses; 5) conducting both intra- and inter-domain contrastive alignment with a focus on the background class in a single contrastive loss. Notably, compared to using a single contrastive loss, utilizing two separate losses inevitably increases the computation burden. The results indicate that our method outperforms all five alternative settings. Additionally, the findings demonstrate that the source prototype is informative and contributes positively to our class-focused contrastive alignment.

Influence of different amounts of point annotations.

Table V highlights a key comparison of two aspects. First, it reveals that as the number of center point labels increases, our model shows improved results. With supervision from 100% of the center points, our model achieves a Dice score of 93.4%, which is just 0.2% lower than that of the fully supervised oracle, as presented in Table I. However, annotating all center points remains time-consuming and requires extensive expert knowledge [12]. In contrast, our model, utilizing only 15% of the center points as the annotation, strikes a good balance of segmentation performance and annotation efficiency. Second, our model consistently outperforms the WDA-Net across varying amounts of target annotations.

Robustness to sample deviations. In Fig. 5, we investigate the impact of the location deviation of the point annotations, i.e., annotation noises. Specifically, we introduced

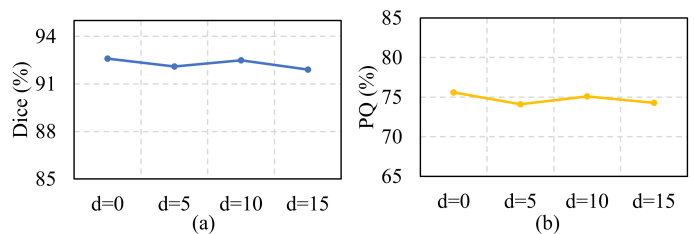


Fig. 5. Robustness to location deviations of the sparse point annotation. The performance of our model (15%) on EPFL Hippocampus→MitoEM-R is evaluated when randomly displacing the sparse point annotations by d pixels from their respective centers.

TABLE VI

INFLUENCE OF THE SAMPLE DEVIATIONS OF THE SPARSE POINT ANNOTATION. THE PERFORMANCE OF OUR MODEL (15%) ON EPFL HIPPOCAMPUS→MITOEM-R WITH DIFFERENT SAMPLING WAS EVALUATED.

	Dice (%)	PQ (%)
Sample 1	92.6	76.1
Sample 2	92.6	75.6
Sample 3	92.4	75.5
Sample 4	92.5	75.6
Sample 5	92.4	75.6
Mean±Std	92.5±0.1	75.8±0.3

by randomly displacing the original point annotations by d pixels from their respective centers, while ensuring that all deviations remain within the foreground object instances. The comparison results in Fig. 5 indicate that our model (15%) shows robust resilience to annotation noises, which is desirable for facilitating efficient annotation processes.

In Table VI, we further examine the influence of sampling deviation on our model’s performance. Specifically, we trained our model (15%) with multiple samples and assessed its performance accordingly. The comparative results demonstrate that the performance of our model shows a standard deviation of 0.1 in Dice and 0.3 in PQ, highlighting the robustness of our model against sampling variations.

Influence of the temperature parameter τ . Table VII illustrates the influence of the temperature parameter τ in the contrastive alignment loss $\mathcal{L}_{contrast}$, where τ controls the softness of the softmax function and also influences the penalty strength on hard negative samples in the contrastive loss [41]. Notably, $\tau=1$ refers to the standard softmax function, while $\tau < 1$ means a more sharpening function and $\tau > 1$ means a more soft function. Table VII shows that the proposed model obtains the highest performance when the temperature parameter τ is 0.1. For our default setting $\tau=0.5$, the model also shows relatively higher performance in Dice.

V. DISCUSSION AND CONCLUSION

This study focuses on segmenting mitochondria from nano-scale electron microscopy (EM) images using a WDA-based approach. Quantitative analysis of subcellular organelles, particularly mitochondria play critical roles in cellular homeostasis and various diseases, including cardiovascular diseases,

TABLE VII
INFLUENCE OF THE TEMPERATURE PARAMETER τ .

	0.05	0.1	0.5	0.7	1.0	1.5
Dice (%)	92.5	92.8	92.6	92.5	92.5	92.3
PQ (%)	75.3	76.5	75.6	75.5	75.9	75.8

neurodegenerative disorders, and cancers [42]. Quantitative information about the morphology, distribution, and number is crucial for the development of therapeutic strategies [3].

To segment numerous mitochondria from EM images, the proposed approach integrates instance-aware pseudo-labeling and class-focused contrastive alignment within a multitask learning framework. To effectively segment numerous mitochondria instances from EM images, our method employs an auxiliary center detection mechanism to improve the quality of the segmentation pseudo-labels. Our framework constructs foreground-class-focused prototypes, which employ the prototypes of the source foreground class to enhance the learning of latent representations. By using just a few center points as additional weak labels, our method outperforms SOTA WDA and UDA methods as well as SAM-like methods in terms of both class-level and instance-level metrics by a large margin. Moreover, we achieve performance close to the supervised upper bound with minimal annotation cost, which is essential for the quantitative analysis of various types of EM images from different species in real-world scenarios.

Despite the greatly reduced annotation cost on the target domain, our method still relies on source data and the corresponding dense labels for model training, which is a limitation in real-world scenarios with privacy concerns. In further work, we will investigate the WDA under the source-free setting.

DECLARATIONS

The authors declare that they have no known competing financial interests or personal relationships that could have appeared to influence the work reported in this paper.

- [1] A. Aswath, A. Alshahaf, B. N. Giepmans, and G. Azzopardi, "Segmentation in large-scale cellular electron microscopy with deep learning: A literature survey," *Medical Image Analysis*, p. 102920, 2023.
- [2] A. Lucchi, Y. Li, and P. Fua, "Learning for structured prediction using approximate subgradient descent with working sets," in *Proceedings of IEEE Conference on Computer Vision and Pattern Recognition*, 2013, pp. 1987–1994.
- [3] K. Neikirk, E.-G. Lopez, A. G. Marshall, A. Alghanem, E. Krystofiak, B. Kula, N. Smith, J. Shao, P. Katti, and A. O. Hinton Jr, "Call to action to properly utilize electron microscopy to measure organelles to monitor disease," *European Journal of Cell Biology*, p. 151365, 2023.
- [4] B. C. Jenkins, K. Neikirk, P. Katti, S. M. Claypool, A. Kirabo, M. R. McReynolds, and A. Hinton, "Mitochondria in disease: changes in shapes and dynamics," *Trends in Biochemical Sciences*, 2024.
- [5] J. Liu, J. Qi, X. Chen, Z. Li, B. Hong, H. Ma, G. Li, L. Shen, D. Liu, Y. Kong *et al.*, "Fear memory-associated synaptic and mitochondrial changes revealed by deep learning-based processing of electron microscopy data," *Cell Reports*, vol. 40, no. 5, 2022.
- [6] O. Ronneberger, P. Fischer, and T. Brox, "U-net: Convolutional networks for biomedical image segmentation," in *International Conference on Medical Image Computing and Computer-Assisted Intervention*, 2015, pp. 234–241.
- [7] J. Peng and Z. Luo, "Cs-net: Instance-aware cellular segmentation with hierarchical dimension-decomposed convolutions and slice-attentive learning," *Knowledge-Based Systems*, vol. 232, p. 107485, 2021.
- [8] Y. Pan, N. Luo, R. Sun, M. Meng, T. Zhang, Z. Xiong, and Y. Zhang, "Adaptive template transformer for mitochondria segmentation in electron microscopy images," in *Proceedings of the IEEE/CVF International Conference on Computer Vision*, 2023, pp. 21 474–21 484.
- [9] S. K. Zhou, H. Greenspan, C. Davatzikos, J. S. Duncan, B. Van Ginneken, A. Madabhushi, J. L. Prince, D. Rueckert, and R. M. Summers, "A review of deep learning in medical imaging: Imaging traits, technology trends, case studies with progress highlights, and future promises," *Proceedings of the IEEE*, vol. 109, no. 5, pp. 820–838, 2021.
- [10] Q. Chen, M. Li, J. Li, B. Hu, and Z. Xiong, "Mask rearranging data augmentation for 3d mitochondria segmentation," in *International Conference on Medical Image Computing and Computer-Assisted Intervention*. Springer, 2022, pp. 36–46.
- [11] R. Shi, L. Duan, T. Huang, and T. Jiang, "Evidential uncertainty-guided mitochondria segmentation for 3d em images," in *Proceedings of the AAAI Conference on Artificial Intelligence*, vol. 38, no. 5, 2024, pp. 4847–4855.
- [12] D. Qiu, S. Xiong, J. Yi, and J. Peng, "Weakly-supervised cross-domain segmentation of electron microscopy with sparse point annotation," *IEEE Transactions on Big Data*, 2024.
- [13] D. Wei, Z. Lin, D. Franco-Barranco, N. Wendt, X. Liu, W. Yin, X. Huang, A. Gupta, W.-D. Jang, X. Wang *et al.*, "Mitomem dataset: Large-scale 3d mitochondria instance segmentation from em images," in *International Conference on Medical Image Computing and Computer-Assisted Intervention*. Springer, 2020, pp. 66–76.
- [14] S. Ben-David, J. Blitzer, K. Crammer, A. Kulesza, F. Pereira, and J. W. Vaughan, "A theory of learning from different domains," *Machine Learning*, vol. 79, pp. 151–175, 2010.
- [15] J. Yang, K. Zhou, Y. Li, and Z. Liu, "Generalized out-of-distribution detection: A survey," *International Journal of Computer Vision*, vol. 132, no. 12, pp. 5635–5662, 2024.
- [16] G. Pekurnaz and X. Wang, "Mitochondrial heterogeneity and homeostasis through the lens of a neuron," *Nature Metabolism*, vol. 4, no. 7, pp. 802–812, 2022.
- [17] H. Guan and M. Liu, "Domain adaptation for medical image analysis: a survey," *IEEE Transactions on Biomedical Engineering*, vol. 69, no. 3, pp. 1173–1185, 2021.
- [18] J. Peng, J. Yi, and Z. Yuan, "Unsupervised mitochondria segmentation in em images via domain adaptive multi-task learning," *IEEE Journal of Selected Topics in Signal Processing*, vol. 14, no. 6, pp. 1199–1209, 2020.
- [19] N. Araslanov and S. Roth, "Self-supervised augmentation consistency for adapting semantic segmentation," in *Proceedings of the IEEE/CVF Conference on Computer Vision and Pattern Recognition*, 2021, pp. 15 384–15 394.
- [20] S. Wu, C. Chen, Z. Xiong, X. Chen, and X. Sun, "Uncertainty-aware label rectification for domain adaptive mitochondria segmentation," in *24th International Conference on Medical Image Computing and Computer Assisted Intervention*. Springer, 2021, pp. 191–200.
- [21] D. Yin, W. Huang, Z. Xiong, and X. Chen, "Class-aware feature alignment for domain adaptive mitochondria segmentation," in *International Conference on Medical Image Computing and Computer-Assisted Intervention*. Springer, 2023, pp. 238–248.
- [22] W. Huang, X. Liu, Z. Cheng, Y. Zhang, and Z. Xiong, "Domain adaptive mitochondria segmentation via enforcing inter-section consistency," in *International Conference on Medical Image Computing and Computer-Assisted Intervention*. Springer, 2022, pp. 89–98.
- [23] D. Qiu, J. Yi, and J. Peng, "Wda-net: Weakly-supervised domain adaptive segmentation of electron microscopy," in *2022 IEEE International Conference on Bioinformatics and Biomedicine (BIBM)*. IEEE, 2022, pp. 1132–1137.
- [24] A. Das, Y. Xian, D. Dai, and B. Schiele, "Weakly-supervised domain adaptive semantic segmentation with prototypical contrastive learning," in *Proceedings of the IEEE/CVF Conference on Computer Vision and Pattern Recognition*, 2023, pp. 15 434–15 443.
- [25] G. Lee, C. Eom, W. Lee, H. Park, and B. Ham, "Bi-directional contrastive learning for domain adaptive semantic segmentation," in *European Conference on Computer Vision*. Springer, 2022, pp. 38–55.
- [26] Y. Tsai, W. Hung, S. Schuler, K. Sohn, M. Yang, and M. Chandraker, "Learning to adapt structured output space for semantic segmentation," in *IEEE Conference on Computer Vision and Pattern Recognition*, 2018, pp. 7472–7481.
- [27] A. Kirillov, E. Mintun, N. Ravi, H. Mao, C. Rolland, L. Gustafson, T. Xiao, S. Whitehead, A. C. Berg, W.-Y. Lo *et al.*, "Segment anything," in *Proceedings of the IEEE/CVF international conference on computer vision*, 2023, pp. 4015–4026.

- [28] J. Wu, Z. Wang, M. Hong, W. Ji, H. Fu, Y. Xu, M. Xu, and Y. Jin, "Medical sam adapter: Adapting segment anything model for medical image segmentation," *Medical image analysis*, vol. 102, p. 103547, 2025.
- [29] M. Long, Y. Cao, J. Wang, and M. Jordan, "Learning transferable features with deep adaptation networks," in *International Conference on Machine Learning*. PMLR, 2015, pp. 97–105.
- [30] Y. Ganin, E. Ustinova, H. Ajakan, P. Germain, and H. Larochelle, "Domain-adversarial training of neural networks," *Journal of Machine Learning Research*, vol. 17, no. 1, pp. 2096–2030, 2016.
- [31] T. Li, S. Roy, H. Zhou, H. Lu, and S. Lathuilière, "Contrast, stylize and adapt: Unsupervised contrastive learning framework for domain adaptive semantic segmentation," in *Proceedings of the IEEE/CVF Conference on Computer Vision and Pattern Recognition*, 2023, pp. 4869–4879.
- [32] J. Hoffman, E. Tzeng, T. Park, J.-Y. Zhu, P. Isola, K. Saenko, A. Efros, and T. Darrell, "Cycada: Cycle-consistent adversarial domain adaptation," in *International Conference on Machine Learning*. PMLR, 2018, pp. 1989–1998.
- [33] Y. Zou, Z. Yu, B. Kumar, and J. Wang, "Domain adaptation for semantic segmentation via class-balanced self-training," in *European Conference on Computer Vision*, 2018, pp. 289–305.
- [34] S. Paul, Y.-H. Tsai, S. Schuler, A. K. Roy-Chowdhury, and M. Chandraker, "Domain adaptive semantic segmentation using weak labels," in *16th European Conference on Computer Vision*. Springer, 2020, pp. 571–587.
- [35] Y. Zhang, Y. Wang, Z. Fang, H. Bian, L. Cai, Z. Wang, and Y. Zhang, "Dawn: Domain-adaptive weakly supervised nuclei segmentation via cross-task interactions," *IEEE Transactions on Circuits and Systems for Video Technology*, vol. 35, no. 5, pp. 4753–4767, 2024.
- [36] Y. Li, Y. Xue, L. Li, X. Zhang, and X. Qian, "Domain adaptive box-supervised instance segmentation network for mitosis detection," *IEEE Transactions on Medical Imaging*, vol. 41, no. 9, pp. 2469–2485, 2022.
- [37] Y. Zhang, D. Zhou, S. Chen, S. Gao, and Y. Ma, "Single-image crowd counting via multi-column convolutional neural network," in *Proceedings of the IEEE Conference on Computer Vision and Pattern Recognition*, 2016, pp. 589–597.
- [38] D.-H. Lee *et al.*, "Pseudo-label: The simple and efficient semi-supervised learning method for deep neural networks," in *Workshop on challenges in representation learning at International Conference on Machine Learning*, vol. 3, no. 2, 2013, p. 896.
- [39] N. Kumar, R. Verma, S. Sharma, S. Bhargava, A. Vahadane, and A. Sethi, "A dataset and a technique for generalized nuclear segmentation for computational pathology," *IEEE Transactions on Medical Imaging*, vol. 36, no. 7, pp. 1550–1560, 2017.
- [40] A. Kirillov, K. He, R. Girshick, C. Rother, and P. Dollár, "Panoptic segmentation," in *Proceedings of the IEEE Conference on Computer Vision and Pattern Recognition*, 2019, pp. 9404–9413.
- [41] F. Wang and H. Liu, "Understanding the behaviour of contrastive loss," in *Proceedings of the IEEE/CVF Conference on Computer Vision and Pattern Recognition*, 2021, pp. 2495–2504.
- [42] C. L. Alston, M. C. Rocha, N. Z. Lax, D. M. Turnbull, and R. W. Taylor, "The genetics and pathology of mitochondrial disease," *The Journal of pathology*, vol. 241, no. 2, pp. 236–250, 2017.